Discover Nano

RESEARCH Open Access

# Xenes-based QCM sensors: exploring borophene and silicene for humidity sensing

Ahmet Gulsaran[1,2*†], Bersu Bastug Azer[1,2*†], Gamze Gursu[4,7], Cihat Tasaltin[8], Nevin Tasaltin[4,5,6,7], Dogu Ozyigit[1,2], A.-Reum Kim[2,3], Boxin Zhao[3], Michael A. Pope[2,3] and Mustafa Yavuz[1,2*]

†Ahmet Gulsaran and Bersu Bastug Azer have contributed equally to this work.

*Correspondence:
Ahmet Gulsaran
agulsaran@uwaterloo.ca
Bersu Bastug Azer
bbastuga@uwaterloo.ca
Mustafa Yavuz
myavuz@uwaterloo.ca

Full list of author information is available at the end of the article

**Abstract**

Borophene and silicene, two novel members of the Xene family, feature high surface reactivity and stability suitable for sensing applications. However, the gas sensing capabilities of these materials in their pristine form have not been systematically investigated. Here we show that borophene- and silicene-based quartz crystal microbalance (QCM) sensors achieve stable and sensitive relative humidity detection and we model their adsorption–desorption mechanisms. Borophene and silicene nanosheets were synthesized via liquid-phase exfoliation and characterized by transmission electron microscopy (TEM), X-ray photoelectron spectroscopy, and Brunauer–Emmett–Teller surface area analysis. The QCM sensors exhibited sensitivities of 3.2 Hz/%RH and 3.9 Hz/%RH, response/recovery times of 122/65 s and 47/130 s and hysteresis of 1.8% and 3.8% hysteresis for borophene and silicene, respectively. The dominant sensing mechanism was determined to be chemisorption, supported by thermodynamic modeling. These results suggest that 2D borophene and silicene can significantly contribute to sensing applications, especially in environments requiring air stability.

**Keywords** Borophene, Silicene, Humidity sensing, Quartz crystal microbalance, Chemisorption

## 1 Introduction

Two-dimensional (2D) materials have gained significant scientific interest due to their unique behaviors, which are not observed at the bulk scale. Notably, applications are being developed across various fields [1]. Just over 20 years ago, in 2004, Novoselov and Geim reported the discovery of graphene, the first 2D carbon material with exceptional electrical properties, high surface area, biocompatibility, and chemical stability. Due to its 2D nature, graphene has its atoms positioned on the surface, which makes it highly sensitive to molecular absorption and interactions. These unique properties of graphene gave rise to significant interest in 2D structures, expanding research into the synthesis and characterization of other 2D materials beyond carbon [2]. As graphene gains more attention worldwide, 2D-Xenes have recently emerged as new "cousins" of graphene and members of the flatland family. Xenes (X = B, Si, Ge, etc.), including borophene, silicene,

© The Author(s) 2025. **Open Access** This article is licensed under a Creative Commons Attribution-NonCommercial-NoDerivatives 4.0 International License, which permits any non-commercial use, sharing, distribution and reproduction in any medium or format, as long as you give appropriate credit to the original author(s) and the source, provide a link to the Creative Commons licence, and indicate if you modified the licensed material. You do not have permission under this licence to share adapted material derived from this article or parts of it. The images or other third party material in this article are included in the article's Creative Commons licence, unless indicated otherwise in a credit line to the material. If material is not included in the article's Creative Commons licence and your intended use is not permitted by statutory regulation or exceeds the permitted use, you will need to obtain permission directly from the copyright holder. To view a copy of this licence, visit http://creativecommons.org/licenses/by-nc-nd/4.0/.

germanene, and phosphorene are pseudoplanar 2D materials composed of group III to IV elements. Unlike graphene, they are not perfectly 2D but instead exhibit buckling, with atomic-scale warping that makes them nearly flat [3]. Borophene, the lightest member in the Xene family with a single layer of boron, is very promising owing to its unique electronic [4], mechanical [5], superconductive [6], and thermal [7] properties. These properties are suitable for several advanced technological applications, such as energy storage [8], gas sensing [9], and catalysis [10]. After more than a decade of theoretical predictions, borophene was experimentally synthesized in 2015 using chemical vapor deposition (CVD) on Ag(111) substrates by both Guisinger's [11] and Wu's group [12], separately. Monolayer borophene synthesis via CVD is costly, time-consuming, and challenging, requiring extensive process optimization and specialized vacuum infrastructure. Addressing these challenges required new approaches, leading to the 2018 development of solution-based methods like low-layer sonication for physical exfoliation [13]. By avoiding the need for expensive equipment or facilities, this approach offers a more affordable solution [14]. Just as borophene's synthesis validated years of theoretical predictions, silicene similarly transitioned from theory to practice. In 1994, Takeda and Shiraishi explored Si and Ge analogues of graphite, describing silicene's low-buckled structure [15]. More than a decade later, in 2007, Guzmán-Verri and Lew Yan Voon officially named it silicene and demonstrated that it is a zero-gap semiconductor [16]. Although silicene's remarkable electronic properties were predicted theoretically, large-scale synthesis was only achieved in 2012 by Vogt et al. on an Ag(111) substrate [17]. Since then, silicene has shown potential in fundamental research and applications in electronics, energy storage, sensors, electrodes, and topological qubits [18].

Understanding the surface physico-chemical properties of borophene and silicene is essential for advancing their practical applications in gas and humidity sensing. The interaction between 2D monolayers and adsorbed molecules plays an important role in determining their sensing performance. While heterostructures of graphene, borophene, silicene, and other 2D materials have been extensively studied for gas detection, the surface properties of pristine borophene and silicene have not been studied in detailed. These materials hold significant potential for gas and humidity sensing due to their high surface-to-volume ratio, which enhances the adsorption of gas molecules. Their remarkable air stability [19] and high carrier mobility [20] further make them ideal candidates for humidity sensors [21, 22]. Various sensing platforms, including capacitive [23], resistive [9], quartz crystal microbalance (QCM) [24], surface acoustic wave (SAW) [25], and micro-electromechanical systems (MEMS) [26], are available for humidity sensor development. While resistance-based platforms are the most common for Xenes due to their high charge carrier mobilities, thermodynamic properties can also be effectively measured using QCM sensors [27]. Moreover, QCM sensors offer distinct advantages, including high sensitivity, stability, and ease of commercial availability [28, 29].

In this study, we successfully prepared 2D borophene and silicene nanosheets through liquid-phase exfoliation, a technique chosen for its cost-efficiency and its ability to eliminate the need for expensive vacuum systems. After verifying the material properties of the synthesized films using scanning electron micsocopy (SEM), transmission electron microscopy (TEM), X-ray photoelectron spectroscopy (XPS), contact angle, and Brunauer–Emmett–Teller (BET) measurements, QCM-based humidity sensors were fabricated by spin-coating the 2D films. The humidity-sensing properties of the sensors

were investigated at room temperature, revealing sensing performance that was comparable to existing literature, including sensitivity, response and recovery times, and hysteresis. Additionally, the humidity sensing mechanism was modeled using both chemisorption and physisorption adsorption models, and thermodynamic parameters of borophene and silicene were calculated by assuming the Langmuir model, for the first time. Our results highlight the environmental stability of these materials and their potential for a wide range of sensing applications.

## 2 Experimental

### 2.1 Synthesis of xenes

Borophene and silicene in this study were prepared by a simple and green sonication method as shown in Fig. 1a while commercial graphene powder ($\mathrm{ProCene}^{\mathrm{TM}}$), with a 99% carbon composition, was supplied from GrapheneCR for the study. Boron powder (95% purity, 1.5 µm) and silicon microparticles (95% purity, 2 µm) were obtained from Nanografi.

For the borophene preparation, 100 mg of boron powder was dissolved in 100 mL of DMF. The mixture was sonicated in a sonication reaction vessel under a nitrogen atmosphere at 200 W for 3 h using a tip sonicator. After sonication, the solution was decanted and subjected to a two-step centrifugation at 5000 rpm and 12,000 rpm for 30 min each. The resulting borophene supernatant was dried in a vacuum oven at 50 °C for 12 h to obtain the final product [30].

For silicene synthesis, 100 mg of silicon microparticles was sonicated in a 50 mL:50 mL mixture of isopropyl alcohol (IPA) and deionized water in a beaker at 200 W for 4 h. Nitrogen was continuously flowed through the booth to prevent oxidation during the

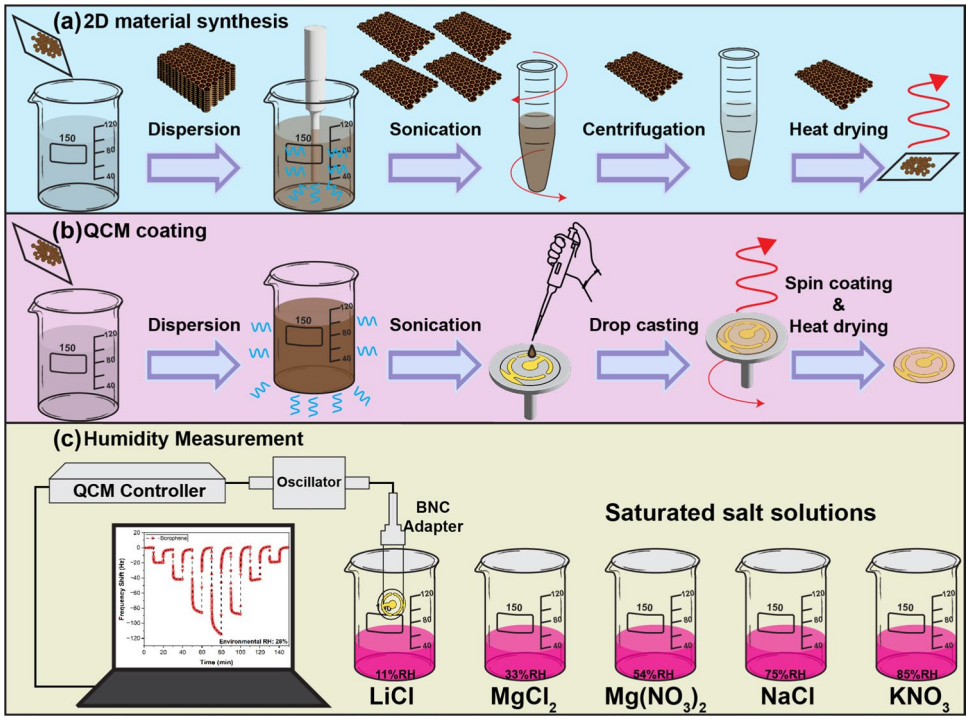



**Fig. 1** Schematics of the experimental method: **a** 2D material synthesis, **b** QCM sensor coating, and **c** humidity sensing measurements

exfoliation process. The exfoliated particles were centrifuged at 5000 rpm and 12,000 rpm for 15 min each. Finally, the silicene nanosheets were carefully collected and dried in a vacuum chamber at 50 °C for 2 h [31].

### 2.2 Sensor fabrication

The snythesized Xenes were dispersed in the isopropanol with a ratio of 5 mg:1 mL. Then the solution was sonicated for 30 min. One inch diameter 5 MHz AT-cut quartz crystals, coated with optically flat polished gold electrodes on both sides, were purchased from Stanford Research Systems (SRS, Stanford, USA). The active area and sensitivity factor of the crystal are $A$ = 0.4 $\mathrm{cm}^2$ and $C_f$ = 56.6 $\mathrm{Hz.cm}^2$ $\mu\mathrm{g}^{-1}$, respectively. The QCM quartz was rinsed sequentially with acetone, isopropanol, and deionized water, and then dried by nitrogen flow. 60 µL of solution was drop casted on the quartz crystal and spin coated at 2000 rpm for 30 s. The coated sensors were then dried under vacuum at 80 °C. These processes (Fig. 1b) were repeated twice to get enough thickness with uniformity.

### 2.3 Characterization

The sheet morpology and porous structure of the prepared 2D materials were examined by a field emission SEM (Hitachi SU8700) at an accelariton voltage of 1–2 kV. The crystallinity and morphology of Xenes were investigated by high-resolution TEM (HRTEM) at the University of Waterloo's QNFCF facility using a JEOL JEM-F200 S/TEM at 200 kV with non-CS corrected, cold field emission (CFEG) emitter and up to $\times$2.0 M magnification. The Xene powders were fixed to a carbon film supported on a copper grid. Characterization of the chemical state of the Xenes was performed by XPS using a Thermo ESCALAB 25 with an Al-K$\alpha$ X-ray source. The wettability of Xene films was investigated using the static contact angle measurement technique by the sessile drop technique. The static contact was imaged using a FASTCAM Mini AX high-speed camera (Photron) and a Resolv4K lens (Navitar) with a 4$\times$ Olympus objective. Images processed via MATLAB and ImageJ identified the contact line and fitted a maximum circle to measure wetting parameters. The specific surface area was determined using a Gemini VII 2390 surface area analyzer (Micromeritics Instrument Corporation) with nitrogen as the adsorbate gas.

### 2.4 Experimental setup

The humidity sensing experimental setup is illustrated in Fig. 1c. Each cycle included 10 min of exposure to a specific RH, followed by 10 min at 11 %RH. Supersaturated solutions of LiCl, $\mathrm{MgCl}_2$, Mg($\mathrm{NO}_3$), NaCl, and $\mathrm{KNO}_3$ provided RH levels of 11%, 33%, 54%, 75%, and 85%, respectively. The humidity salts, with $\geq$99.0% purity, were supplied by Sigma-Aldrich. Resonance frequency was recorded by the QCM200 controller, connected to a PC via RS-232. The frequency counter had a 0.1 Hz resolution with 1 s gate. The SRS200 controller logged the QCM sensor's frequency response to varying RH levels using an oscillator circuit. As the response/recovery times and sensitivity can be changed with the operating temperature [32], all the experiments were carried out at room temperature (22.5 °C) and atmospheric pressure environment inside 200 mL glass beakers of supersaturated solutions. To obtain frequency shifts, the resonance frequency at 11 %RH was used as the baseline. Response/recovery times (11–85 %RH) were

defined by the time to reach 90% of steady-state, assumed after 10 min. Hysteresis was calculated as the largest difference between adsorption and desorption frequency shifts.

## 3 Results and discussion

### 3.1 Characterization results

The morphological analysis of the prepared borophene and silicene sheets, performed by SEM, are shown in Fig. 2.

According to the SEM micrographs, the prepared borophene nanosheets consisted of few layers (Fig. 2a, c), consistent with the previous studies [33]. The magnified images (Fig. 2b, d) illustrate the porous structures of the prepared 2D materials, which can increase the surface area of the films and create more sites for water molecule adsorption. This porous architecture is beneficial for sensing applications, as it enhances the interaction between target molecules and the sensing film surface [34].

The detailed morphology and crystal structure of the borophene and silicene sheets were characterized by TEM. HRTEM imaging are presented in Fig. 3a and e. The white circled areas were zoomed to investigate atomic structure (Fig. 3b, f) and the corresponding fast Fourier transform (FFT) (Fig. 3d, h) diffraction patterns of the synthesized borophene and silicene sheets confirm the crystalline nature.

For borophene, the d-spacing is calculated as 0.47 nm and 0.48 from the lattice fringe of HRTEM imaging (Fig. 3c) and the corresponding FFT diffraction pattern (Fig. 3d), respectively. These findings are in good agreement with the literature, both with theoretical calculations (0.50 nm) [35] and experimental measurements (0.51 nm), corresponding to the (104) plane of a $\beta$-rhombohedral B structure [36]. For silicene, the d-spacing is calculated as 0.33 nm from both the lattice fringe of HRTEM imaging (Fig. 3g) and the

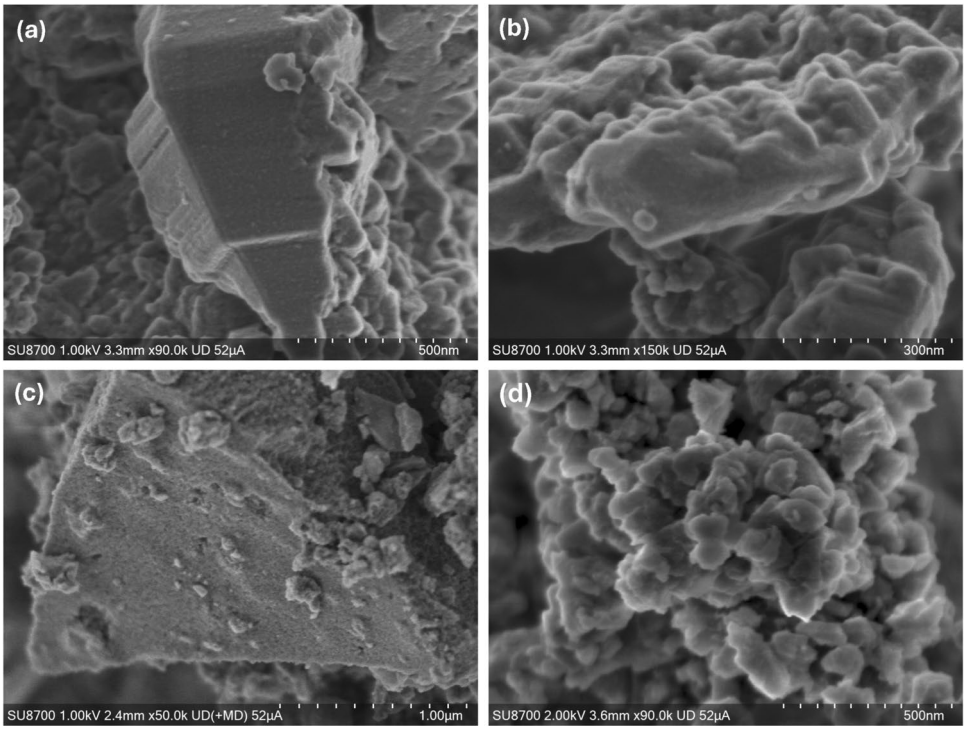



**Fig. 2** SEM characterization of 2D materials: **a**, **c** SEM images of borophene and silicene sheets, respectively; **b**, **d** Corresponding high-magnification images revealing their porous surface structures

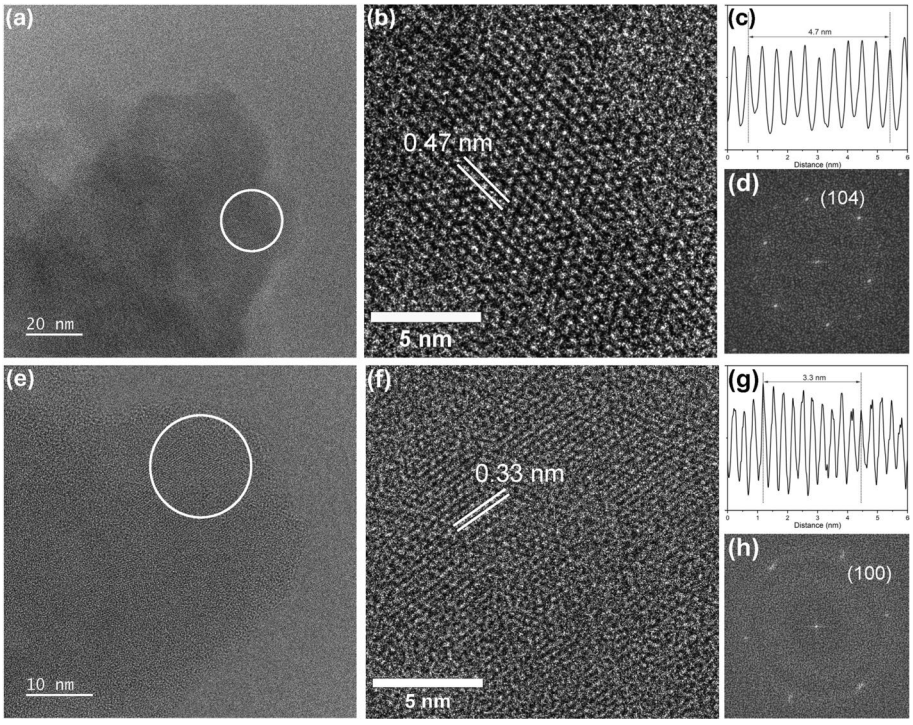



**Fig. 3** TEM imaging of 2D materials: **a**, **e** TEM images of borophene and silicene sheets, respectively; **b**, **f** magnified views of the circled regions in (**a**) and (**e**) showing the crystal structures; **c**, **g** colormaps aligned with the crystal directions to extract atomic spacing; and **d**, **h** FFT patterns corresponding to (**b**) and (**f**), respectively

corresponding FFT diffraction pattern (Fig. 3h). These findings are well aligned with the literature (0.34 nm), corresponding to the (100) plane of a honeycomb hexagonal lattice of Si atoms [37]. The FFT patterns consist of different circles of spots, each containing six spots arranged in hexagonal symmetry (Fig. 3d, h). These findings are characteristic of borophene and silicene, confirming the single-crystal nature of the sheets. This also suggests the pristinity of the well-crystallized 2D sheets after the exfoliation processes.

The surface compositions and chemical states of the sythesized films were investigated using XPS spectra, and the binding energy calibration was referenced to C 1 s at 284.6 eV. XPS survey (Fig. S1a) scans over binding energies ranging from 0 to 1400 eV. XPS survey spectra indicate that the surfaces synthesized films are clean with only a trace amount of carbon due to air exposure.

For borophene, Fig. S1a shows the boron 1 s signal, as well as carbon 1s and O 1s peaks. Three peaks can be resolved in the boron 1 s signal in Fig. 4a, 191.60, 188.25 and 187.03 eV, indicating the three types of boron atom with various chemical environments. Since the binding energy of the boron 1 s peak in bulk boron is 189.4 eV [38], the two peaks at lower binding energies (188.25 and 187.03 eV), slightly redshifted compared to the bulk value, are likely attributed to B–B bonds in the 2D sythnesized borophene sheets. In contrast, the higher energy peak (191.60 eV) is associated to boron oxidation [39] and the measured area ratio of the B–O peak to B–B peak is quite negligible, indicating that most boron atoms remain unoxidized. The two B–B peaks (188.25 and 187.03 eV) can be explained by two types of bonding structures with different chemical environments in 2D borophene sheets [12].

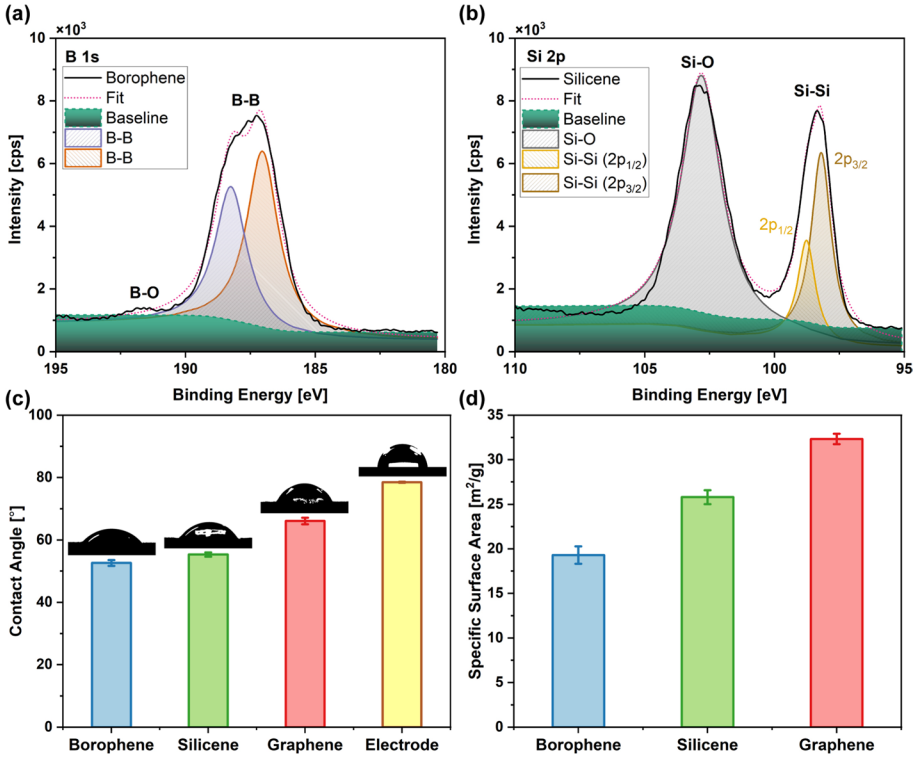



**Fig. 4** Material characterization results: **a** XPS spectra illustrating B 1 s peak for borophene, **b** Si 2p peak for silicene, **c** contact angles measured for borophene, silicene, graphene, and the bare electrode, and **d** BET surface area values for borophene, silicene, and graphene

For silicene, silicon 2p signal, as well as carbon 1s and O 1s peaks are observed as shown in Fig. S1a. In the silicon 2p signal given in Fig. 4b, three distinct peaks are observed at 102.82, 98.77, and 98.20 eV, representing three types of silicon atoms with different chemical environments. Given that the binding energy of the silicon 2p peak in bulk silicon is 99.3 eV [38], the two peaks at lower binding energies (98.77 and 98.20 eV) are slightly redshifted relative to the bulk value and are likely associated with Si-Si bonds in the 2D synthesized silicene sheets. On the other hand, the higher energy peak (102.82 eV) corresponds to silicon oxidation [40], and the area ratio of the Si–O peak to the Si–Si peak suggests the oxidation formation. XPS is a surface-sensitive technique and reveals that silicene tends to oxidize into atomically thin $SiO_2$ when exposed to air [41]. The Si–O signal observed is likely due to this surface oxidation. However, the persistence of silicene-like Si–Si bonding in the surface composition indicates that the quality of the prepared 2D nanosheets remains intact. In fact, silicene can even maintain its honeycomb structure even when its surface is completely covered by oxygen adatoms [42]. The two Si–Si peaks (98.77 and 98.20 eV) can be explained by Si $2p_{1/2}$ and $2p_{3/2}$ being the spin-orbit doublets of Si-Si, respectively [43].

As shown in Fig. S1a, both the carbon 1 s signal and the O 1 s peak are detected for graphene. Our XPS analysis indicates the presence of two component peaks in the C1s peak, located at 284.55 and 285.31 eV, given in Fig. S1b. The peak at the lower binding energy (284.55 eV) is associated with C–C $sp^2$ bonding in graphene [44]. The peak of $sp^3$ carbon atoms in carbon films has a higher energy than $sp^2$, with an energy difference $\Delta$ E of approximately 0.9 eV according to the literature [45]. This difference matches well

with our measurements (0.76 eV). Therefore, the peak at 285.31 eV can be attributed to $sp^3$ C–C bonding carbon.

In conclusion, XPS analysis of the synthesized 2D materials reveals clean surfaces with minimal contamination. Borophene shows unoxidized boron with two distinct B–B bonding environments. Silicene exhibits surface oxidation to $SiO_2$, but retains the Si–Si bonding, indicating high-quality 2D sheets. Graphene displays typical C–C $sp^2$ and $sp^3$ bonding. These findings confirm the successful synthesis of these materials and their suitability for further study and application.

To evaluate each films' water absorption ability, the water contact angle tests were conducted. The water contact angles for borophene, silicene, graphene, and bare gold electrode were found as $52.60°$, $55.33°$, $66.07°$, and $78.49°$, respectively, as given in Figs. 4c and S2. Any contact angle lower than $90°$ describes the system to have water on a hydrophilic surface [46]. Therefore, achieving lower angles for borophene and silicene compared to graphene and bare gold electrode suggests that both surfaces of borophene and silicene are more hydrophilic therefore enabling them to detect humidity more effectively [47]. However, no significant difference of the contact angle was observed between borophene and silicene. Besides the hydrophilicity, the specific surface area also plays an important role in humidity sensing performance.

In order to quantify the specific surface area of the prepared nanostructures, BET analyses were conducted. The specific surface areas of borophene, silicene, and graphene were calculated to be 19.3, 25.8, and 32.3 $m^2/g$, respectively, as shown in Fig. 4d. Silicene has a larger specific surface area than borophene, which provides more adsorption sites and higher sensitivity.

To determine the functional groups of the 2D nanostructures, Fourier-transform infrared spectroscopy (FTIR) analysis were conducted in our previous reports for both borophene[48] and silicene[31]. Several stretching vibrations including B-B, B-H, B-O, C=O, and B-O-B were detected in our previous work for borophene[48] matching with the other reports[49]. Similar to borophene, various characteristic FTIR peaks appeared of silicene such as $CH_x$, Si–O–Si, Si–O, and Si–C consistent with the literature [50]. Additionally, corresponding FTIR spectrum confirms the existence of surface–OH groups which might play a role in humidity sensing. In combination with the XPS analysis, the presence of oxygen-containing functional groups of the synthesized 2D structures were confirmed with FTIR spectra.

To show the quality of the prepared borophene[51] and silicene[52], bandgaps were calculated optically in our previous works. Theoretically, borophene shows metallic properties without a bandgap [53]. However, the bandgap can reach up to 0.5 eV due to shear strains [54]. In fact, a bandgap up to 2.1 eV can be reached by varying the sheet thickness of borophene. [55] The bandgap energy for the prepared borophene of 0.94 eV in our previous work[51] matches well with the literature considering practical constraints. The theoretical bandgap of pristine silicene is smaller than 0.1 eV. [56] However, this bandgap can go up to 0.5 eV by surface adsorption of alkali metal. [57] Moreover, the bandgap of the silicene depends on the oxidation state and reported up to 1.2 eV [42, 58]. In our earlier work [52], the bandgap energy of the synthesized silicene was found to be 0.84 eV which is in agreement with other studies. Hence, achieving smaller bandgaps than 1 eV for both borophene and silicene matching with the literature is a quantitative

parameter including the factors such as low contamination, low oxidation, low shear strains, and reasonable sheet thickness.

X-ray diffraction (XRD) analyses were performed to determine the crystal structure of the synthesized borophene [59] and silicene [52] in our earlier studies. According to borophene's XRD result, no phase change from the physical exfoliation process from boron microparticles to borophene was observed. Borophene were indexed to the centrosymmetric $\beta$-rhombohedral borophene crystal structure [11, 13, 36]. Similar to the borophene, XRD results of silicene confirm high purity silicene with no pattern belonging to any other elements proving no contamination from the synthesis. The diffraction peaks indicate centrosymmetric cubic crystals for the prepared silicene.

The physical and colloidal stabilities of the prepared borophene were verified with sufficient electrostatic repulsion via zeta potential measurements [48] and dynamic light scattering (DLS) measurements [5] in our previous works, respectively. Additionally, Raman spectroscopy characterization is planned as future work to identify the number of layers.

### 3.2 Humidity sensing characteristic

A humidity environment of 11–85% relative humidity was created using saturated salt solutions. During the test, the ambient temperature is 22.5 °C, the sampling interval is 0.1 s and the switching time of the humidity bottle is 600 s. The dynamic curves of the borophene and silicene QCM humidity sensors are plotted in Fig. 5a and d, respectively. It can be seen that the frequency shift of both sensors increases with increasing humidity.

The results show that the resonant frequency of the borophene and silicene QCM sensors decreases with increasing relative humidity, which is attributed to the increased mass of the 2D films on the QCM electrode surface caused by the adsorption of water molecules. The frequency of both sensors stabilizes over time at each humidity level. They exhibit an exponential-like behavior, with a significant shift initially before settling to a steady-state value. An overshoot behavior was observed for silicene, which has also been reported in the literature for borophene [21].

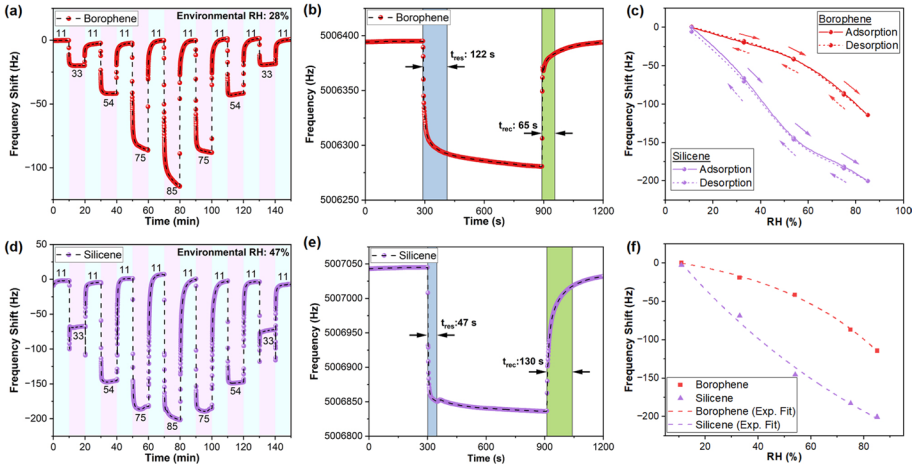



**Fig. 5** Humidity sensing performance: **a**, **d** Frequency response of borophene and silicene sensors under different RH conditions; **b**, **e** response and recovery times; **c** hysteresis behavior; and **f** frequency shift vs. RH fitting curves for both sensors

Figure 5f represents the fitting curves of the sensors at 11–85 %RH. The functional relationships of borophene and silicene are $\Delta f = 25.0 - 19.7e^{2.31\times \mathrm{RH}}$ and $\Delta f = -378.4 - 423.7e^{1.03\times \mathrm{RH}}$ where $\Delta f$ is in Hz units with the correlation coefficients ($R^2$) of 0.999 and 0.994, respectively. As shown in Fig. 5f, borophene exhibits higher sensitivity at elevated humidity levels, while silicene shows greater sensitivity at lower humidity levels. The increased sensitivity of borophene at high RH matches with the findings in the literature [22]. The frequency shifts of the borophene and silicene humidity sensors are −114.6 Hz and −208.9 Hz, respectively. The significantly larger frequency shift observed for the silicene sensor indicates a stronger moisture response, suggesting that silicene is more sensitive to humidity.

The higher sensitivity aligns well with the results from the materials characteristics given in Fig. 4. Both borophene and silicene exhibit similar hydrophilicity (Fig 4c), as indicated by their nearly identical contact angles. However, silicene offers a higher specific surface area compared to borophene (Fig 4d), which enhances its interaction with the surrounding environment by providing more adsoprtion sites. Additionally, silicene tends to form more oxide layer on its surface (Fig 4a, b), further contributing to its reactivity. The oxidation of silicene creates a porous, highly sensitive structure [60], while defects in silicene enhance binding strength [61]. These factors make silicene more sensitive to humidity changes than borophene, as the increased surface area and oxide layer allow for greater adsorption and interaction with water molecules. Therefore, silicene proves to be a more promising material for humidity sensing applications.

Figure 5b and e show the response and recovery times of both sensors. The response and recovery times for the borophene and silicene sensors are 122.1/65.0 s and 47.1/130.1 s, respectively. It is important to note that the RH environments created by saturated salt solutions require time to stabilize, which could add some extra time to the response and recovery time estimations. Borophene exhibited faster desorption compared to adsorption, while silicene showed quicker adsorption than desorption. Since borophene and silicene showed opposite characteristics in terms of the higher sensitivity region and quicker response/recovery time (one showed higher sensitivity at high temperature with faster recovery time, while the other showed higher sensitivity at lower humidity levels with faster response time), there might be a correlation between the regions of higher sensitivity and faster response/recovery times.

The adsorption and desorption curves for the borophene and silicene sensors are shown in Fig. 5c. The maximum humidity hysteresis is 1.8% for borophene at 75 %RH and 3.8% for silicene at 33 %RH. Both materials exhibit higher hysteresis at the humidity levels where they demonstrate greater sensitivity. Thus, higher sensitivity corresponds to higher hysteresis in these sensors.

The comparison of sensing performance between the QCM humidity sensor in this work and those reported in previous studies with similar performance is provided in Table 1.

Given that response and recovery times can be influenced by experimental conditions, the humidity range for each measurement is included in parentheses. The results show that the presented sensors exhibit comparable sensitivity, response and recovery times, and hysteresis in humidity sensing to those reported in the literature. Prior work shows that borophene's sensitivity can be increased by 90 times with $ZrO_2$ [22] and by 27 times

**Table 1** Humidity sensing performance of QCM sensors in this work compared with other studies presenting similar sensing characteristics

| Material | Range (%RH) | Sensitivity (Hz/%RH) | Res./Rec. time (s) | Hysteresis (%) | References |
|---|---|---|---|---|---|
| DNA | 0–70 | 0.53 | – | – | [62] |
| PVA | 11–58 | 3.51 | 15/9 (11–84) | – | [63] |
| GO fiber | 10–90 | 2.98 | 130/36 (20–80) | 6.6 | [64] |
| UFR/nano-silica | 11–84 | 5.3 | 12/25 (11–84) | 1.3 | [65] |
| S-$Ti_3C_2$( MXene) | 11–97 | 11.3 | 15/6 (40–97) | 1.2 | [66] |
| PVA/ZnO | 10–90 | 0.74 | – | – | [67] |
| ZnO NP | 11–97 | 1.0 | – | – | [27] |
| ZnO NW | 11–97 | 0.4 | – | – | [27] |
| $TiO_2$ | 0–20 | 7.5 | 120/240 (0–20) | | [68] |
| ZIF-67 | 11–97 | 3.52 | 3/3 (40–97) | – | [69] |
| ZIF-CoNi | 11–97 | 6.52 | 3/4 (40–97) | – | [69] |
| BiOCl | 11–97 | 7.3 | 5.2/4.5 (11–85) | 2 | [70] |
| Graphite | 11–97 | 2.38 | 8/5 (11–75) | – | [71] |
| Borophene | 11–85 | 3.2 | 122/65 (11–85) | 1.8 | This work |
| Silicene | 11–85 | 3.9 | 47/130 (11–85) | 3.8 | This work |

with graphene heterojunctions [21]. Introducing similar heterojunctions could lead to substantial improvements in the performance of these QCM sensors.

It should be noted that no stable humidity response was observed for the graphene-coated QCM humidity sensor, with the best observed response shown in Fig. S3. This suggests that the impact of moisture on graphene is not straightforward. As reported by Hou et al. [21], the sensitivity of graphene-based humidity sensors was 26 times lower than that of borophene. This lower sensitivity may explain the lack of stable humidity sensing performance for graphene. In contrast, both borophene and silicene exhibited repeatable and consistent results with respect to humidity. Therefore, borophene and silicene are promising candidates for applications exposed to open air, as they demonstrate stable humidity responses, unlike graphene, where the effects of varying humidity levels are difficult to predict.

To the best of our knowledge, these 2D materials have not been used plain for sensing applications due to challenges in creating uniform films, which often leads to inferior performance unless polymers or nanocomposites are incorporated. Consequently, their standalone sensing mechanisms are still unexplored. Therefore, it is essential to investigate the adsorption and desorption mechanisms and extract their thermodynamic properties. The outcomes can contribute improving the future applications of these materials.

### 3.3 Humidity sensing mechanism

The interaction between water molecules and the surface of 2D films plays a significant role in the adsorption and desorption processes. The surfaces of borophene and silicene are sensitive to atmospheric moisture due to their high reactivity with water molecules as shown by the presence of surface–OH groups observed in FTIR spectroscopy [31, 48] and the hydrophilic behavior demonstrated by contact angle measurements (Fig. 4c). Additionally, the presence of oxide states observed in XPS further enhances the surface's affinity for water (Fig. 4a, b).

Hence, water molecules can be easily adsorbed onto the surface, either through hydrogen bonding or as dissociated $H_2O$ species. This leads to the formation of a skin layer with surface-adsorbed water molecules. The adsorbed water can be categorized into two

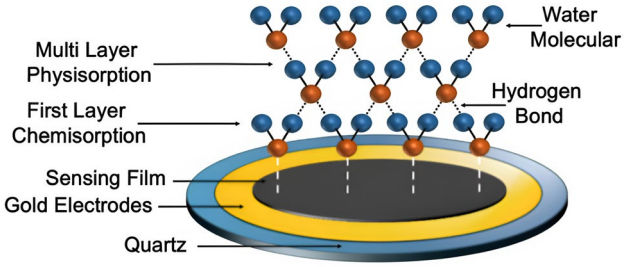



**Fig. 6** Schematics of the humidity sensing mechanism

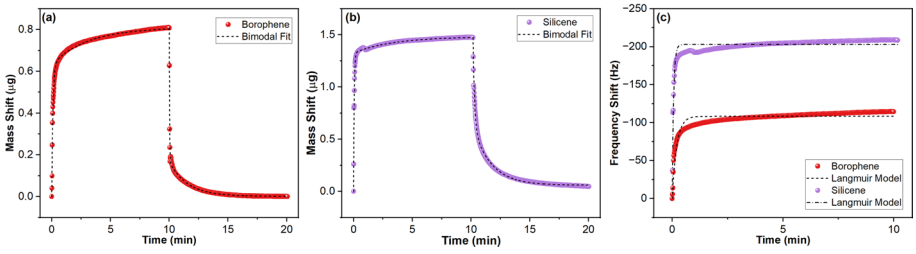



**Fig. 7** Plots of the humidity sensing mechanism: **a**, **b** Adsorbed and desorbed mass for borophene and silicene, fitted with bimodal chemisorption and physisorption models, and **c** Langmuir adsorption isotherm fitting of frequency shifts for both sensors from 11 %RH to 85 %RH

types: (1) chemisorbed water, which consists of water species with limited mobility near the solid surface, and (2) physisorbed water, which is loosely adsorbed, highly mobile, and can exchange slowly with gaseous water molecules in air as shown Fig. 6 [67].

As shown in Fig. 6, the interaction between moisture and the surface could be described by a first chemisorbed layer and physisorbed multi-molecular layers. To model the adsorption and desorption characteristics of humidity, a two-step first-order kinetics model derived by Ferreira and Rubner [72] was employed as shown in Eq. (1). This model assumes that substrate effects are minimal and that the kinetics of adsorption are independent of both the number of layers already deposited and the properties of the substrate.

$$\Delta m = A_c \left(1 - e^{-t/\tau_c}\right) + A_p \left(1 - e^{-t/\tau_p}\right) \tag{1}$$

where $A_c$ and $A_p$ are the mass absorbance constants and $\tau_c$ and $\tau_p$ are the time constants for chemisorption and physisorption, respectively. The first exponential corresponds to a first-order kinetics with a very short characteristic time (approximately 5–10 s) where the second process has longer times ranging from 100 to 350 s [73].

The mass change per unit area is related to the frequency shift can be obtained by using the Sauerbrey equation [74].

$$\Delta f = -C_f \Delta m \tag{2}$$

where $\Delta f$, $C_f$, and $\Delta m$ are the frequency change, the sensitivity factor (56.6 Hz $\mu g^{-1}$ $cm^2$), and change in mass unit area, respectively. By combining the active area and the sensitivity factor provided by the supplier, a mass change sensitivity of $-141.5$ Hz/μg was obtained. The adsorbed and desorbed mass change responses of borophene and silicene between 11 and 85 %RH are plotted in Fig. 7a and b.

As can be seen from the plots, the chemisorption and physisorption model (Eq. 1) greatly fitted ($R^2 > 0.99$) to the experimental data. The fitted mass absorbance ($A_c$ for chemisorption, $A_p$ for physisorption)and time constants ($\tau_c$ for chemisorption, $\tau_p$ for physisorption) are given in Table 2.

According to Table 2, chemisorption is the dominant adsorption mechanism for both materials, as indicated by $|A_c| > |A_p|$. This observation agrees with earlier research on silicene which identified chemisorption as the primary mechanism through experimental [75] and theoretical [76] investigations.

This suggests that the adsorption model can be even simplified using a single-term, first-order kinetics approach. To further analyze the adsorption, the Langmuir adsorption isotherm was employed as it is a useful model can to extract the key thermodynamic properties of the films, such as adsorption/desorption coefficients and the Gibbs free energy of the process. The Langmuir isotherm is a simplified version of the kinetics model derived by Ferreira and Rubner (Eq. (1)). Instead of using two first-order terms, the Langmuir model uses a single-term expression, as shown in Eq. (3) [27]:

$$\Delta f = \Delta f_{\max} K' \left(1 - e^{-t/\tau}\right) \tag{3}$$

where $K'$ is the association constant and $\tau$ is the relaxation time, defined by:

$$K' = \frac{C}{C + (k_d/k_a)} \tag{4}$$

$$\tau = \frac{1}{k_a C + k_d} \tag{5}$$

Here, $C = 0.981\ \mathrm{mol/m^3}$ is the molar moisture concentration at 85 %RH at 22.5 °C, while $k_a$ and $k_d$ are the Langmuir adsorption and desorption rate constants, respectively.

As shown by the fitting curves in Fig. 7c, a mismatch occurs just before saturation for both structures. The Langmuir adsorption isotherm predicts a steeper increase compared to the experimental data, suggesting that the adsorption process slows down as it approaches saturation. This deviation implies that the experimental conditions do not fully conform to the assumptions of the Langmuir model near saturation. The interaction between moisture and the surface was described by a chemisorbed monolayer followed by physisorbed multilayers, as illustrated in Fig. 6. Therefore, the mismatch is expected due to the dropped physisorption term which is responsible for the slower multilayer interaction. Nevertheless, the fits remain acceptable, with $R^2 > 0.8$, consistent with findings in the literature [27, 77, 78].

To further investigate the kinetic reaction between the 2D films and water molecules, the Gibbs free energy ($\Delta G$) at a constant temperature is given by [27]:

**Table 2** Fitted adsorption and desorption coefficients for the bimodal chemisorption and physisorption models

| Material | $A_c$(μg) | $\tau_c$(s) | $A_p$(μg) | $\tau_p$ (s) |
|---|---|---|---|---|
| Borophene (Adsorption) | 0.63 | 6.4 | 0.18 | 182 |
| Borophene (Desorption) | −0.64 | 1.7 | −0.16 | 94 |
| Silicene (Adsorption) | 1.32 | 3.0 | 0.16 | 205 |
| Silicene (Desorption) | −0.86 | 7.4 | −0.56 | 93 |

**Table 3** Langmuir table

| Material | $\Delta f_{max}$ (Hz) | $\Delta m_{max}$ (μg) | $k_a(\mathrm{M^{-1}s^{-1}})$ | $k_d(\times 10^{-3}\mathrm{s^{-1}})$ | $K_{equ}$ | $\Delta G$( kJ/mo) |
|---|---|---|---|---|---|---|
| Borophene | 114.6 | 0.81 | 78.5 | 4.5 | 17.1 | −6.98 |
| Silicene | 208.9 | 1.48 | 256.9 | 7.3 | 34.6 | −8.71 |

$$\Delta G = -RT \ln K_{\mathrm{equ}} \tag{6}$$

where $R$ is the universal gas constant (8.314 J/mol K), $T$ is the temperature (296.65 K), and $K_{\mathrm{equ}} = \frac{k_a C}{k_d}$ is the equilibrium constant. The values of the fitted parameters for Langmuir model are given in Table 3.

The negative Gibbs free energy values of −6.98 kJ/mol and −8.71 kJ/mol for borophene and silicene, respectively, confirm spontaneous adsorption processes. Silicene's more negative value and higher adsorbed mass highlight its superior adsorption capabilities [27]. Material characterization further supports these results by showing silicene's higher specific surface area. These findings consistently explain silicene's higher sensitivity in humidity sensing.

## 4 Conclusion

In this study, borophene and silicene based QCM humidity sensors were successfully developed. The sensing performance of pristine 2D borophene and silicene nanosheets are reported for the first time without the addition of polymeric or composite matrices. 2D borophene and silicene nanosheets were synthesized using liquid-phase exfoliation technique. The synthesized nanosheets were characterized using TEM, XPS, contact angle, and surface area measurements, showing good agreement with previous results. The sensors achieved moderate sensitivities of 3.2 Hz/%RH for borophene and 3.9 Hz/%RH for silicene, with response/recovery times of 122/65 s and 47/130 s, respectively. The hysteresis values were low (1.8% for borophene and 3.8% for silicene), and the sensors demonstrated good repeatability. The dominant sensing mechanism was determined to be chemisorption, with silicene exhibiting a higher adsorption tendency due to its more negative Gibbs free energy and larger specific surface area. These findings indicate that borophene and silicene are promising materials for humidity sensing applications and potentially other fields, such as VOC detection, breath analysis, and wound healing. In fact, the demonstrated stability under varying humidity conditions suggests their suitability for various environmental applications. However, surface oxidation states and number of layers play a crucial role on the sensor performance and the control over both was limited in this work. Therefore, addressing these challenges is essential for further improving and exploring the sensing performance of these materials. Additionally, further research should examine selectivity, long-term stability, and broader application domains, including VOC detection, breath analysis, and biomedical monitoring.

## Supplementary Information

The online version contains supplementary material available at https://doi.org/10.1186/s11671-025-04284-w.

Supplementary file 1 (pdf 711 KB)

**Acknowledgements**
A.G. and B.B.A contributed equally to this work. SEM images were taken at The Ontario Battery and Electrochemistry-research Centre (OBEC). TEM images were taken at University of Waterloo Quantum-Nano Fabrication and Characterization Facility (QNFCF). A.G. and B.B.A acknowledges the contribution of Nicki Shaw, Sandra Gibson, and Nathan Nelson-Fitzpatrick.

**Author contributions**
A.G. and B.B.A contributed equally to this work. A.G. and B.B.A wrote the main manuscript text and prepared the figures. G.G., C.T., and N.T. prepared the 2D materials. D.O., A.K., and B.Z. provided the contact angle measurements and analysis. M.A.P. provided necessary chemicals and lab space when needed. M.Y. supervised the research and provided the resources. All authors reviewed the manuscript.

**Funding**
M.Y. acknowledge the support of Canadian Mathematics of Information Technology and Complex Systems Agency (MITACS) [Grant No: IT17161, 2000-2024], NSERC Alliance [Grant No: ALLRP 554872 - 20] and Discovery [Grant No: GPIN-2020–06053] research programs.

**Data availability**
Data is available from the corresponding authors upon reasonable request.

## Declarations

**Ethical approval and consent to participate**
Not applicable.

**Conflict of interest**
The authors declare no Conflict of interest.

**Consent for publication**
Not applicable.

**Materials availability**
Not applicable.

**Code availability**
Not applicable.

**Author details**
[1]Department of Mechanical and Mechatronics Engineering, University of Waterloo, 200 University Ave. West, Waterloo N2L 3G1, ON, Canada
[2]Waterloo Institute for Nanotechnology (WIN), University of Waterloo, 200 University Ave. West, Waterloo N2L 3G1, ON, Canada
[3]Department of Chemical Engineering, University of Waterloo, 200 University Ave. West, Waterloo N2L 3G1, ON, Canada
[4]Department of Basic Sciences, Maltepe University, Istanbul, Turkey
[5]Department of Renewable Energy Technologies and Management, Maltepe University, Istanbul, Turkey
[6]Environment and Energy Technologies Research Center, Maltepe University, Istanbul, Turkey
[7]CONSENS Inc., Maltepe University Research Center, Istanbul, Turkey
[8]Materials Institute, TUBITAK Marmara Research Center, Kocaeli, Turkey

Received: 18 February 2025 / Accepted: 9 June 2025
Published online: 11 July 2025

**References**

1. Dubertret B, Heine T, Terrones M. The rise of two-dimensional materials. Washington, D.C: ACS Publications; 2015.
2. Novoselov KS, Geim AK, Morozov SV, Jiang D-E, Zhang Y, Dubonos SV, Grigorieva IV, Firsov AA. Electric field effect in atomically thin carbon films. Science. 2004;306(5696):666–9.
3. Ranjan P, Lee JM, Kumar P, Vinu A. Borophene: new sensation in flatland. Adv Mater. 2020;32(34):2000531.
4. Ranjan P, Sahu TK, Bhushan R, Yamijala SS, Late DJ, Kumar P, Vinu A. Freestanding borophene and its hybrids. Adv Mater. 2019;31(27):1900353.
5. Karapınar IS, Pehlivan AO, Özsoy Özbay AE, Yazgan AU, Taşaltın N, Karakuş S. Improvement of the mechanical properties of cementitious composites by the novel synthesized borophene nanosheets. J Compos Mater. 2022;56(10):1615–30.
6. Gao M, Li Q-Z, Yan X-W, Wang J. Prediction of phonon-mediated superconductivity in borophene. Phys Rev B. 2017;95(2):024505.
7. Sun H, Li Q, Wan X. First-principles study of thermal properties of borophene. Phys Chem Chem Phys. 2016;18(22):14927–32.
8. Rao D, Zhang L, Meng Z, Zhang X, Wang Y, Qiao G, Shen X, Xia H, Liu J, Lu R. Ultrahigh energy storage and ultrafast ion diffusion in borophene-based anodes for rechargeable metal ion batteries. J Mater Chem A. 2017;5(5):2328–38.
9. Wu Z, Liang X, Zhao Z, Wu Q, Liu X, Liu Y, Xu M, Hou C, Tai G. Ultrasensitive and durable borophene-based humidity sensors for advanced human-centric applications. Chem Eng J. 2024;500: 156881.
10. Yang F, Pan Y, Zhu J. Enhanced catalytic activity of noble metal@ borophene/WS2 heterojunction for hydrogen evolution reaction. Appl Surf Sci. 2025;680: 161321.

11. Mannix AJ, Zhou X-F, Kiraly B, Wood JD, Alducin D, Myers BD, Liu X, Fisher BL, Santiago U, Guest JR, et al. Synthesis of borophenes: anisotropic, two-dimensional boron polymorphs. Science. 2015;350(6267):1513–6.
12. Feng B, Zhang J, Zhong Q, Li W, Li S, Li H, Cheng P, Meng S, Chen L, Wu K. Experimental realization of two-dimensional boron sheets. Nat Chem. 2016;8(6):563–8.
13. Li H, Jing L, Liu W, Lin J, Tay RY, Tsang SH, Teo EHT. Scalable production of few-layer boron sheets by liquid-phase exfoliation and their superior supercapacitive performance. ACS Nano. 2018;12(2):1262–72.
14. Hou C, Tai G, Liu Y, Liu X. Borophene gas sensor. Nano Res. 2022;15:1–8.
15. Takeda K, Shiraishi K. Theoretical possibility of stage corrugation in Si and Ge analogs of graphite. Phys Rev B. 1994;50(20):14916.
16. Guzmán-Verri GG, Lew Yan Voon LC. Electronic structure of silicon-based nanostructures. Phys Rev B-Condens Matter Mater Phys. 2007;76(7): 075131.
17. Vogt P, De Padova P, Quaresima C, Avila J, Frantzeskakis E, Asensio MC, Resta A, Ealet B, Le Lay G. Silicene: compelling experimental evidence for graphenelike two-dimensional silicon. Phys Rev Lett. 2012;108(15): 155501.
18. Shan G, Tan H, Ma R, Zhao H, Huang W. Recent progress in emergent two-dimensional silicene. Nanoscale. 2023;15(7):2982–96.
19. Hou C, Tai G, Hao J, Sheng L, Liu B, Wu Z. Ultrastable crystalline semiconducting hydrogenated borophene. Angew Chem Int Ed. 2020;59(27):10819–25.
20. Zhang J-J, Altalhi T, Yang J-H, Yakobson BI. Semiconducting $\alpha$'-boron sheet with high mobility and low all-boron contact resistance: a first-principles study. Nanoscale. 2021;13(18):8474–80.
21. Hou C, Tai G, Liu B, Wu Z, Yin Y. Borophene-graphene heterostructure: preparation and ultrasensitive humidity sensing. Nano Res. 2021;14:1–8.
22. Hou C, Tai G, Liu Y, Wu Z, Wu Z, Liang X. Ultrasensitive humidity sensing and the multifunctional applications of borophene-MoS 2 heterostructures. J Mater Chem A. 2021;9(22):13100–8.
23. Shaukat RA, Khan MU, Saqib QM, Chougale MY, Kim J, Bae J. All range highly linear and sensitive humidity sensor based on 2D material TiSi2 for real-time monitoring. Sens Actuators, B Chem. 2021;345: 130371.
24. Fauzi F, Rianjanu A, Santoso I, Triyana K. Gas and humidity sensing with quartz crystal microbalance (QCM) coated with graphene-based materials-a mini review. Sens Actuators, A. 2021;330: 112837.
25. Su Y, Li C, Li M, Li H, Xu S, Qian L, Yang B. Surface acoustic wave humidity sensor based on three-dimensional architecture graphene/PVA/SiO2 and its application for respiration monitoring. Sens Actuators, B Chem. 2020;308: 127693.
26. Gulsaran A, Azer BB, Saritas R, Kocer S, Shama YS, Rahmanian S, Mouharrar H, Abdelrahman R, Abdel-Rahman E, Yavuz M. High sensitivity, thermal noise-driven aluminum-based resonant mems humidity sensor. Sens Actuators, A. 2024;378: 115844.
27. Asar N, Erol A, Okur S, Arikan M. Morphology-dependent humidity adsorption kinetics of ZnO nanostructures. Sens Actuators, A. 2012;187:37–42.
28. Tang K, Ding X, Yu X, Lu J, Liu F, Li H, Chen X. High fundamental frequency QCM humidity sensor based on C60-OH/Ti3C2TX nanocomposite with superior response. Sens Actuators, B Chem. 2024;426: 137014.
29. Yang J, Feng L, Chen Y, Feng L, Lu J, Du L, Guo J, Cheng Z, Shi Z, Zhao L. High-sensitivity and environmentally friendly humidity sensors deposited with recyclable green microspheres for wireless monitoring. ACS Appl Mater Interfaces. 2022;14(13):15608–22.
30. Baytemir G, Gürol İ, Karakuş S, Taşaltın C, Taşaltın N. Nickel phthalocyanine-borophene nanocomposite-based electrodes for non-enzymatic electrochemical detection of glucose. J Mater Sci: Mater Electron. 2022;33(20):16586–96.
31. Taşaltın N, Taşaltın C, Üstün-Alkan F, Karakuş S. Biocompatible, antibacterial, and antifungal two-dimensional silicene nanosheets with a honeycomb hexagonal structure. Biomass Convers Biorefinery. 2024;14(15):16943–50.
32. Aasi A, Aghaei SM, Bajgani SE, Panchapakesan B. Computational study on sensing properties of Pd-decorated phosphorene for detecting acetone, ethanol, methanol, and toluene-a density functional theory investigation. Adv Theory Simul. 2021;4(11):2100256.
33. Auwärter W. Hexagonal boron nitride monolayers on metal supports: versatile templates for atoms, molecules and nanostructures. Surf Sci Rep. 2019;74(1):1–95.
34. Ţălu. Micro and nanoscale characterization of three-dimensional surfaces. Basics and applications. Cluj-Napoca: Napoca Star Publishing House; 2015. p. 10–2.
35. Ozdogan C, Mukhopadhyay S, Hayami W, Guvenc Z, Pandey R, Boustani I. The unusually stable b100 fullerene, structural transitions in boron nanostructures, and a comparative study of $\alpha$-and $\gamma$-boron and sheets. J Phys Chem C. 2010;114(10):4362–75.
36. Ji X, Kong N, Wang J, Li W, Xiao Y, Gan ST, Zhang Y, Li Y, Song X, Xiong Q, et al. A novel top-down synthesis of ultrathin 2d boron nanosheets for multimodal imaging-guided cancer therapy. Adv Mater. 2018;30(36):1803031.
37. Liu J, Yang Y, Lyu P, Nachtigall P, Xu Y. Few-layer silicene nanosheets with superior lithium-storage properties. Adv Mater. 2018;30(26):1800838.
38. Moudler JF, Stickle WF, Sobol PE, Bomben KD. Handbook of x-ray photoelectron spectroscopy. Eden Prairie: Perkin-Elmer; 1992.
39. Ong CW, Huang H, Zheng B, Kwok R, Hui Y, Lau W. X-ray photoemission spectroscopy of nonmetallic materials: electronic structures of boron and Bx Oy. J Appl Phys. 2004;95(7):3527–34.
40. Himpsel F, McFeely F, Taleb-Ibrahimi A, Yarmoff J, Hollinger G. Microscopic structure of the SiO2/Si interface. Phys Rev B. 1988;38(9):6084.
41. Molle A, Grazianetti C, Chiappe D, Cinquanta E, Cianci E, Tallarida G, Fanciulli M. Hindering the oxidation of silicene with non-reactive encapsulation. Adv Func Mater. 2013;23(35):4340–4.
42. Du Y, Zhuang J, Liu H, Xu X, Eilers S, Wu K, Cheng P, Zhao J, Pi X, See KW, et al. Tuning the band gap in silicene by oxidation. ACS Nano. 2014;8(10):10019–25.
43. Lee C-C, Yoshinobu J, Mukai K, Yoshimoto S, Ueda H, Friedlein R, Fleurence A, Yamada-Takamura Y, Ozaki T. Single-particle excitation of core states in epitaxial silicene. Phys Rev B. 2017;95(11): 115437.
44. Park J, Mitchel WC, Elhamri S, Grazulis L, Hoelscher J, Mahalingam K, Hwang C, Mo S-K, Lee J. Observation of the intrinsic bandgap behaviour in as-grown epitaxial twisted graphene. Nat Commun. 2015;6(1):5677.

45. Díaz J, Paolicelli G, Ferrer S, Comin F. Separation of the sp 3 and sp 2 components in the c1s photoemission spectra of amorphous carbon films. Phys Rev B. 1996;54(11):8064.
46. Ahmad D, Van Den Boogaert I, Miller J, Presswell R, Jouhara H. Hydrophilic and hydrophobic materials and their applications. Energy sour Part A: Recovery Util Environ Effects. 2018;40(22):2686–725.
47. Wang L, Song J, Yu C. MgAl-LDH nanoflowers as a novel sensing material for high-performance humidity sensing. RSC Adv. 2024;14(30):21991–8.
48. Taşaltın C, Türkmen TA, Taşaltın N, Karakuş S. Highly sensitive non-enzymatic electrochemical glucose biosensor based on pani: $\beta$ 12 borophene. J Mater Sci: Mater Electron. 2021;32:10750–60.
49. Ma D, Zhao J, Xie J, Zhang F, Wang R, Wu L, Liang W, Li D, Ge Y, Li J, et al. Ultrathin boron nanosheets as an emerging two-dimensional photoluminescence material for bioimaging. Nanoscale Horiz. 2020;5(4):705–13.
50. Ryan BJ, Hanrahan MP, Wang Y, Ramesh U, Nyamekye CK, Nelson RD, Liu Z, Huang C, Whitehead B, Wang J, et al. Silicene, siloxene, or silicane? revealing the structure and optical properties of silicon nanosheets derived from calcium disilicide. Chem Mater. 2019;32(2):795–804.
51. Yıldız D, Karadeniz S, Yıldırım M, Tasaltın N, Gulsaran A, Bastug Azer B, Yavuz M. Novel pani: Borophene/Si Schottky device for the sensitive detection of illumination and NaCl salt solutions. J Mater Sci: Mater Electron. 2024;35(7):469.
52. Karabulut A, Yıldız D, Yıldırım M, Güllü H, Kocyigit A, Tasaltın N, Gulsaran A, Azer BB, Yavuz M. The effects of Ppy-silicene composite on the performance of n-/p-type silicon semiconductor-based photodiodes. Sens Actuators, A. 2024;379:115996.
53. Kunstmann J, Quandt A. Broad boron sheets and boron nanotubes: an ab initio study of structural, electronic, and mechanical properties. Phy Rev B-Condens Matter Mater Phys. 2006;74(3): 035413.
54. Wang Z-Q, Lü T-Y, Wang H-Q, Feng YP, Zheng J-C. Band structure engineering of borophane by first principles calculations. RSC Adv. 2017;7(75):47746–52.
55. Wang X, Liang J, You Q, Zhu J, Fang F, Xiang Y, Song J. Bandgap engineering of hydroxy-functionalized borophene for superior photo-electrochemical performance. Angew Chem Int Ed. 2020;59(52):23559–63.
56. Drummond N, Zolyomi V, Fal'Ko V. Electrically tunable band gap in silicene. Phys Rev B-Condens Matter Mater Phys. 2012;85(7): 075423.
57. Quhe R, Fei R, Liu Q, Zheng J, Li H, Xu C, Ni Z, Wang Y, Yu D, Gao Z, et al. Tunable and sizable band gap in silicene by surface adsorption. Sci Rep. 2012;2(1):853.
58. Xu X, Zhuang J, Du Y, Feng H, Zhang N, Liu C, Lei T, Wang J, Spencer M, Morishita T, et al. Effects of oxygen adsorption on the surface state of epitaxial silicene on ag (111). Sci Rep. 2014;4(1):7543.
59. Güngör S, Taşaltın C, Gürol İ, Baytemir G, Karakuş S, Taşaltın N. Copper phthalocyanine-borophene nanocomposite-based non-enzymatic electrochemical urea biosensor. Appl Phys A. 2022;128(1):89.
60. Lyuleeva A, Helbich T, Bobinger M, Rieger B, Becherer M, Lugli P, Rivadeneyra A. Functionalized and oxidized silicon nanosheets: customized design for enhanced sensitivity towards relative humidity. Sens Actuators, B Chem. 2019;283:451–7.
61. Hussain T, Kaewmaraya T, Chakraborty S, Ahuja R. Defect and substitution-induced silicene sensor to probe toxic gases. J Phys Chem C. 2016;120(44):25256–62.
62. Murata T, Minami K, Yamazaki T, Yoshikawa G, Ariga K. Detection of trace amounts of water in organic solvents by DNA-based nanomechanical sensors. Biosensors. 2022;12(12):1103.
63. Zheng Z, Zhang G, Wang X, Kong X. Comparative study of gravimetric humidity sensor platforms based on CMUT and QCM. Micromachines. 2022;13(10):1651.
64. Dong H, Le X, Pang K, Pang J, Li D, Xu Z, Gao C, Xie J. A serial flexible humidity sensor based on graphene oxide fibers and quartz crystal resonator. J Micromech Microeng. 2020;31(2): 025004.
65. Lv R, Peng J, Chen S, Hu Y, Wang M, Lin J, Zhou X, Zheng X. A highly linear humidity sensor based on quartz crystal microbalance coated with urea formaldehyde resin/nano silica composite films. Sens Actuators, B Chem. 2017;250:721–5.
66. Li R, Fan Y, Ma Z, Zhang D, Liu Y, Xu J. Controllable preparation of ultrathin MXene nanosheets and their excellent QCM humidity sensing properties enhanced by fluoride doping. Microchim Acta. 2021;188:1–11.
67. Horzum N, Taşçıoglu D, Okur S, Demir MM. Humidity sensing properties of ZnO-based fibers by electrospinning. Talanta. 2011;85(2):1105–11.
68. Addabbo T, Fort A, Mugnaini M, Vignoli V, Baldi A, Bruzzi M. Quartz-crystal microbalance gas sensors based on TiO 2 nanoparticles. IEEE Trans Instrum Meas. 2018;67(3):722–30.
69. Zhang D, Luo N, Xue Z, Bai Y-L, Xu J. Effect of open metal sites in cobalt-based bimetallic metal-organic framework nanoparticles-coated quartz crystal microbalance (qcm) for humidity detection. ACS Appl Nano Mater. 2022;5(2):2147–55.
70. Chen Q, Feng N-B, Huang X-H, Yao Y, Jin Y-R, Pan W, Liu D. Humidity-sensing properties of a BiOCl-coated quartz crystal microbalance. ACS Omega. 2020;5(30):18818–25.
71. Yu X, Chen X, Yu X, Chen X, Ding X. A quartz crystal microbalance (QCM) humidity sensor based on a pencil-drawn method with high quality factor. IEEE Trans Electron Dev. 2021;68(10):5149–54.
72. Ferreira M, Rubner M. Molecular-level processing of conjugated polymers. 1. layer-by-layer manipulation of conjugated polyions. Macromolecules. 1995;28(21):7107–14.
73. Raposo M, Pontes R, Mattoso L, Oliveira O. Kinetics of adsorption of poly (o-methoxyaniline) self-assembled films. Macromolecules. 1997;30(20):6095–101.
74. Sauerbrey G. Verwendung von schwingquarzen zur wägung dünner schichten und zur mikrowägung. Z Phys. 1959;155:206–22.
75. Hu W, Xia N, Wu X, Li Z, Yang J. Silicene as a highly sensitive molecule sensor for NH 3, NO and NO 2. Phys Chem Chem Phys. 2014;16(15):6957–62.
76. Feng J-W, Liu Y-J, Wang H-X, Zhao J-X, Cai Q-H, Wang X-Z. Gas adsorption on silicene: a theoretical study. Comput Mater Sci. 2014;87:218–26.
77. Gao N, Li H-Y, Zhang W, Zhang Y, Zeng Y, Zhixiang H, Liu J, Jiang J, Miao L, Yi F, et al. Qcm-based humidity sensor and sensing properties employing colloidal SnO2 nanowires. Sens Actuators, B Chem. 2019;293:129–35.
78. Zhang D, Wang D, Li P, Zhou X, Zong X, Dong G. Facile fabrication of high-performance QCM humidity sensor based on layer-by-layer self-assembled polyaniline/graphene oxide nanocomposite film. Sens Actuators, B Chem. 2018;255:1869–77.

## Publisher's Note
Springer Nature remains neutral with regard to jurisdictional claims in published maps and institutional affiliations.

## Supplementary Information
The online version contains supplementary material available at https://doi.org/10.1186/s11671-025-04284-w.